A data-model comparative study of ionospheric positive storm phase in the mid-latitude *F*-region

G. Lu[1], L. P. Goncharenko[2], A. J. Coster[2], A. D. Richmond[1], R. G. Roble[1], N. Aponte[3], and L. J. Paxton[4]

[1] High Altitude Observatory, National Center for Atmospheric Research, Boulder, CO

[2] Haystack Observatory, Massachusetts Institute of Technology, Westford, MA

[3] Arecibo Observatory, Arecibo, PR

[4] Johns Hopkins University, Applied Physics Laboratory, Laurel, MD

Abstract. A strong positive storm phase was observed by both the Millstone Hill and Arecibo incoherent scatter radars during a moderate geomagnetic storm on 10 September 2005. The positive storm phase featured a peculiar UT-altitude profile of the *F*-region electron density enhancement that closely resembles the Greek letter Λ. The radar measurements showed that the uplifting of the electron density peak height corresponded to a strong upward ion drift whereas the subsequent falling of the peak height coincided with a downward ion drift. Using realistic, time-dependent ionospheric convection as input, the Thermosphere-Ionosphere Electrodynamics General Circulation Model (TIEGCM) is able to reproduce the same Λ-like structure in the electron density profile, along with many large-scale features in electron temperature and vertical ion drift as observed by the radars. The model also captures the temporal and spatial TEC variations as shown in the global GPS maps. The comparison with the GUVI O/N_2 ratio is less satisfactory, although there is a general agreement in terms of relative O/N_2 ration changes during the storm in the longitudinal sector between 60°W and 80°W where the radars are located. The detailed data-model comparison carried out in this study is

helpful not only to validate the model but also to interpret the complex observations. An important finding of the study is that it is the enhanced meridional neutral wind, not the penetration electric fields, that is the primary cause of the peculiar Λ structure of the *F*-region electron density profile.

1. Introduction

Ionospheric disturbances are often categorized as a positive or negative storm phase if there is an increase or decrease of the *F*-region peak electron densities with respect to their quiet time values. It is well known that ionospheric storm effects are determined by a combination of chemical, dynamical, and electrodynamical processes. Increased O_2 and N_2 densities result in increased conversion of O^+ to O_2^+ and NO^+, which then rapidly recombine with electrons, resulting in a rapid decrease in electron density [*Rishbeth*, 1989; *Burns et al*., 1995]. Although neutral composition changes are often attributed to the formation of a negative storm phase [*Prolss*, 1993], several studies have shown a positive storm phase as a result of a large increase in the O/N_2 ratio [e.g., *Burns et al*., 1995; *Field et al*., 1998]. Large dawn-to-dusk electric fields associated with a strongly southward interplanetary magnetic field (IMF) are most effective in producing large geomagnetic storms. They drive strong ion convection in the high latitude polar regions, and a fraction of magnetospheric electric field can penetrate to mid and low latitudes, prompting nearly simultaneous ionospheric disturbances there. The fasting-moving ions driven by magnetospheric electric fields at high latitudes collide with neutrals to produce frictional heating or Joule heating. The excessive Joule heating dissipation in the high-latitude polar regions produces large pressure gradients that drive neutral winds equatorward toward mid and low latitudes, even into the opposite hemisphere. An enhanced equatorward (poleward) meridional wind pushes plasma up (down) along magnetic field lines due to their inclination with respect to Earth's surface, raising or lowering the *F*-region electron density peak height accordingly. In addition, a polarization electric field can be created by the storm-enhanced neutral winds to form the “disturbance dynamo”

effect [*Blanc and Richmond*, 1980].

While the effects of neutral wind dynamics on ionospheric storms are fully recognized [see reviews by *Prolss*, 1995; *Buonsanto,* 1999], in recent years more attention has been paid to the prompt penetration electric fields, due partly to the fact that major geomagnetic storms tend to be associated with a strong southward IMF. *Huang et al*. [2005a] showed several cases in which the penetration electric field can last several hours after the IMF turns southward and geomagnetic activity remains high. The large penetration electric fields produce the so-called "super-fountain effect" which significantly intensities the dayside total electron content (TEC) [e.g., *Tsurutani et al*., 2004; *Mannucci et al*., 2005], and are found to be the primary cause of the dayside positive storm phase [e.g., *Huang et al*., 2005b]. Therefore, the storm effects produced by such long-lasting penetration electric fields may have overshadowed the relatively weaker effects by disturbance neutral winds during major storms.

In this paper, we present a case study of a dayside positive storm phase during a moderate geomagnetic storm event that occurred on 10 September 2005. The event is particular interesting because a very peculiar UT-altitude profile of the F-region electron density that closely resembles the Greek letter Λ. We show a detailed comparison of the simulations from the Thermosphere-Ionosphere Electrodynamics General Circulation Model (TIEGCM) [*Richmond et al*., 1992] with measurements obtained from two incoherent scatter radars located in Millstone Hill and Arecibo, as well as with those from the global GPS receivers and the TIMED/GUVI instrument. Through such a comprehensive data-model comparison, we not only validate our model's performance but also shed some new light on the underlying physical processes that are responsible for a peculiar *F*-region electron density variation.

2. Observations and Model Comparison

2.1 Geophysical conditions and model inputs

The solar wind and geophysical conditions for the period of 8-10 September 2005 are shown in Figure 1. The solar wind parameters measured by the ACE satellite have been time-shifted by 36 mins to account for the nominal solar wind propagation time from the upstream location the magnetopause. From 0400 UT on 8 September until ~ 1400 UT on 9 September, the magnitude of IMF B_z was less than 5 nT. As a result, the geophysical condition of the ionosphere and magnetosphere was quiet, as indicated by the small values of *Dst*, *AE*, the polar-cap potential drop, and the power inputs of Joule heating and auroral precipitation. Around 1400 UT on 9 September, an interplanetary shock arrived, along with a rapid increase in the solar wind dynamic pressure. The pressure impulse prompted a storm sudden commencement as shown by the positive excursion in *Dst*, together with increases in *AE*, the polar-cap potential drop and Joule heating dissipation. The geophysical disturbances associated with the solar wind dynamic pressure impulse are interesting. But in this study we will focus our attention on the disturbance during the second half day on 10 September when a moderate geomagnetic storm took place following a southward turning of the IMF B_z near 1600 UT. The storm had a minimum *Dst* value of about -70nT and a maximum *AE* value of ~2500nT. The cross-polar-cap potential drop and the hemispheric integrated Joule heating were increased as well after the IMF turned southward. The magnitude of the hemispheric integrated Joule heating rate was much larger in the northern hemisphere than in the southern hemisphere. This hemispheric difference is due in part to the relatively sparse data coverage in the southern hemisphere which resulted in smaller electric potential drops as shown in Figure 1e [also see *Lu et al*., 1996]. The increase in auroral electron energy flux was rather subtle, and the hemispheric integrated auroral power was substantially smaller than Joule heating dissipation during the event.

Ionospheric convection and auroral precipitation are two of the important upper boundary inputs to the TIEGCM. To simulate the ionospheric and thermospheric response to this moderate geomagnetic storm we have used the realistic, time-dependent high-latitude ionospheric convection and auroral

precipitation patterns derived from the assimilative mapping of ionospheric electrodynamics (AMIE) procedure [*Richmond and Kamide*, 1988]. The AMIE patterns in the northern and southern hemispheres were derived from various space and ground based observations, including those from the DMSP (F13, 15, and 16) and NOAA (NOAA-15, 16, and 17) satellites, 12 SuperDARN radars (10 in the northern hemisphere and 2 in the southern hemisphere), and 178 ground magnetometers. The AMIE patterns had in a 5-min cadence and were timely interpolated to drive the TIEGCM, which ran in a 2-min time step. Solar EUV and UV fluxes were obtained from the empirical flare irradiance spectral model (FISM) [*Chamberlin et al*., 2007] to replace the traditional F10.7 proxy for this particular event, and the amplitudes of diurnal and semi-diurnal tides at the model's lower boundary were based on the Global Scale Wave Model (GSWM) [*Hagan and Forbes*, 2002].

2.2 Comparison with Radar Measurements

Figure 2 shows the measured and simulated electron density *Ne*, electron temperature *Te*, and vertical ion drift over Millstone Hill from 10-24 UT on the quiet of 8 September (left column) and on the storm day of 10 September (right column), respectively. The Millstone Hill radar is located at 42.6°N and 288.5°E, and the local time (LT) corresponds roughly to UT-5. In comparison with the quiet-day Ne distribution, there was a significant increase of *Ne* in the *F*-region between ~1600 and 2300UT during the storm on 10 September, along with the increase of the *F*-region peak height (or h_mF_2.) The most striking feature is the UT-altitude profile of the *Ne* enhancement which closely resembles the Greek letter Λ. Accompanied by the increase in *Ne* was a decrease in *Te*. *A*nti-correlation between *Te* and *Ne* is fully anticipated since the electron cooling rate is proportional to *Ne* [*Schunk and Nagy*, 2000]. The ion temperature (not shown), on the other hand, increased slightly during the storm [*Goncharenko et al*., 2007]. The measured vertical ion drift showed a large upward motion starting ~1640UT, which coincided with the initial uplift of h_mF_2. The ion drift became downward at about

1900 UT, about the same time when h_mF_2 started to fall.

At first glance, the TIEGCM simulations appear to be in a good quantitative agreement with the Millstone Hill radar measurements on both quiet and storm days. A similar Λ-like structure in the UT-altitude distribution of *Ne* is very well reproduced by the model, as is the anti-correlation between the simulated *Ne* and *Te*. There are, however, some qualitative differences between the observed and simulated *Ne*. For example, the simulated *F*-region *Te* on 8 September starts to decrease too fast compared to the radar measured *Te* shown in the 3rd row. But on the storm day of 10 September, the simulations show a general good agreement with the measurements, except for a short period around 2200 UT when the simulated *Te* becomes cooler than the measured *Te* by a few hundreds of degree. The simulated vertical ion drifts also show many large-scale features consistent with the radar observations at both locations. On the quiet day as well as prior to the storm onset, the Millstone Hill radar observed upward ion drifts above ~350 km. Similar upward ion drifts are seen in the simulations but at a higher altitude, mostly above 450 km. The prestorm upward ion drift, as found in the simulations, is associated with ion diffusion. At 1640 UT, the time when the Millstone Hill radar started to observe strong upward ion drift, the simulation also shows an temporarily enhanced upward drift above 300km followed a more pronounced upward ion drift about 10 minutes later. In the region below 250 km, the simulated strong upward ion drift (> 25 m/s) is nearly 40 minutes lagging behind the radar measurements, though these lower-altitude ion drifts have little effect on the peculiar *F*-region electron density profile.

Figure 3 shows the similar data-model comparison over Arecibo. The Arecibo radar is at 18.3°N and 293.3°E, and LT=UT-4.4. It observed a similar Λ-like structure in the *Ne* profile as the Millstone Hill radar did. The rising of h_mF_2 at Arecibo, however, was delayed until ~1750UT, again coincident with the enhanced upward ion drift. The time delay in the initial uplifting of h_mF_2 between Millstone Hill and Arecibo implies a propagation speed of 680 m/s for the traveling ionospheric disturbances.

The anti-correlation between *Ne* and *Te* was more pronounced in the Arecibo measurements.

The simulated *Ne* is in a reasonably good agreement with the radar measurement. But the simulations do not show the measured temporal density drop around 2100 UT on 8 September, and the simulated N*e* is also too large compared to the measured *Ne* in the upward lag of the Λ structure. The simulated *Te* is also in a good agreement with the measured *Te* on both the quiet and storm days. The simulated vertical ion drift agrees well with the measurements on 8 September. On 10 September, the prestorm *F*-region vertical ion drift consisted of a strong downward flow, followed by a strong upward flow. The simulations display a similar downward-to-upward change in vertical ion drift; but the transition occurs ~1 hour too early with respect to the radar observations. A better agreement between the measured and simulated drifts is found after 1800 UT over Arecibo, including the hockey-stick like structure of strong upward ion drift followed by downward ion drift.

2.3 Comparison with GPS TEC Measurements

Figure 4 shows the comparison between the GPS TEC measurements and the simulated TEC from the TIEGCM. These TEC maps are plotted in a fixed local time range between 4 and 20 LT as there was not much activity on the nightside. Although the GPS TEC maps suffer from the lack of data over the vast Pacific and Atlantic oceans, some storm-related TEC changes were discernible, particularly over the Central and North American sector (highlighted by the square box) and in the South Pacific region (highlighted by the oval-shape area). There was a gradual increase in TEC in both these regions, with a maximum TEC value reached around 2100 UT on 10 September.

There are some similarities between the simulated and observed TEC features, such as the TEC enhancements in the American and South Pacific regions. In the GPS maps, the TEC enhancement over the South Pacific appeared as a locally confined structure; in the model, it appears as a westward, slow-

moving structure originated near the western edge of South America. From 1700 UT to 2100 UT, near central America the observed TEC increased from ~30 TECU to over 70 TECU; in the simulation, TEC increases from ~25 TECU to ~50 TECU. An important difference between the GPS TEC maps and the simulated TEC maps is that the measured TEC values in the mid- and low-latitude regions are about 15~35% larger than the simulations. This underestimation is simply due to the altitude limit of the TIEGCM (the upper boundary altitude was about 570 km for this storm which took place under near solar-minimum condition).

2.4 Comparison with GUVI O/N_2 Measurements

Figure 5 shows the percent difference distributions of the O/N_2 ratio, with the GUVI measurements shown on the top, and the simulation results that have been spatially and temporally extracted along the satellite track shown on the bottom. Again, the comparison represents the percent change of O/N_2 on 10 September with respect to the quiet day of 8 September. There is some degree of agreement between the measurements and simulation in terms of general morphology. For example, a depletion of O/N_2 over most parts of the northern and southern polar region and a moderate increase (~10%) for most of the mid-to-low latitude region; an increase of O/N_2 is seen at the northern edge of Canada as well as between the longitude range of 120°W ~ 160°W, although the model results appear as much larger scale structures. There was a ~20% increase just eastward of the US east cost; a similar O/N_2 increase can be seen in the simulation as well, but slightly further eastward. In general, the agreement is reasonable in the longitude sector between 60°W and 80°W where the Millstone Hill and Arecibo radars are located. There are, of course, many qualitative differences between the measurements and simulations, particularly a pair of positive and negative O/N_2 changes over North America in the simulation which cannot be found in the GUVI data.

3. Discussion

The detailed data and model comparison shown in the previous section assure us that the coupled AMIE-TIEGCM has captured reasonably well some large-scale storm features in the *F* region. In this section, we attempt to explore the underlying physical mechanisms responsible to the observed ionospheric storm effects with the help of the numerical simulations.

As pointed out in the Introduction, neutral composition changes are known to play an important role in producing ionospheric disturbances during geomagnetic storms. To verify whether the composition change is a controlling factor in this case, Figure 6 shows the altitude-UT profiles of the percent changes in electron density and in the O/N_2 ratio with respect to the quite reference day of 8 September 2005. The comparison reveals no direct correlation between the electron density increase and the O/N_2 enhancement, indicating that the composition changes were not the main cause of this particular positive storm phase. This is consistent with the finding by *Goncharenko et al.* [2007], who concluded that the O/N_2 ratio change played only a minor role in the case.

We now turn our attention to the possible effect that dynamical and electrodynamical processes may have on the observed ionospheric disturbances. The simulated vertical ion drift shown in the bottom rows of Figures 2 and 3 is the sum of all contributions from the electric fields, meridional neutral wind, and ion diffusion [i.e., *Schunk and Nagy*, 2000]. In order to assess the relative contribution of neutral wind and the electric fields to vertical ion drift, Figure 7 shows, from top to bottom, the meridional wind, the vertical ion drift component due to the meridional wind, and the vertical ion drift due to electric field. As expected, the wind-driven vertical ion drift and the meridional wind are anti-correlated in the mid-latitude region. Compared to the total vertical ion drift shown in the bottom rows of Figures 2 and 3, it is evident that storm-time vertical ion drifts are primarily driven by the meridional wind surges. There are no significant changes in the electric field driven ion drift except for a very brief period around 1640 UT in both Millstone Hill and Arecibo. This temporal increase in

upward ion drift is a result of the magnetospheric electric field penetration to mid latitudes. But this leakage/penetration of magnetospheric electric field is a numerical rather than a well-simulated physical effect since the model was not coupled with an inner magnetospheric model such as in the study by *Maruyama et al.* [2005]. This weak penetration electric field, however, did produce a simultaneous increase in TEC seen by several ground GPS receivers across several latitudes at 1630 UT [*Goncharenko et al.,* 2007]. The penetration electric field in our simulation is thus delayed about 10 minutes compared to observations, which can partly be attributed to the fact that the TIEGCM outputs were saved in a 10-min cadence although the model itself was running in a 2-min time step.

Figure 8 shows the UT-latitude distributions of selected variables at 350 km along 70°W. These difference plots illustrate the changes of the fields during storm time on September 10 with respect to those during the relatively quiet condition on September 8. There is a clear signature of traveling atmospheric disturbances (TADs) in meridional wind, propagating at a phase speed of ~700 m/s as highlighted by the slanted dashed line. However, the meridional wind itself is much slower, with a peak speed at ~100 m/s. Figure 8b shows the vertical ion drift component associated with neutral wind. The equatorward wind surge shown in Figure 8a pushed ions upward in the northern hemisphere and downward in the southern hemisphere, with the demarcation at ~12°S which corresponds to the magnetic equator at 70°W. The UT-latitude distribution of the wind-driven vertical ion drift has the same propagation phase speed as the TADs in meridional wind. The disturbed meridional wind is predominantly from the northern hemisphere into the southern hemisphere, even though the storm event took place near equinox. Two facts may have contributed to the hemispheric asymmetry in the simulations: (1) as shown in Figure 1, the simulated total Joule heating dissipation during the storm interval was much larger in the northern hemisphere than in the southern hemisphere, and (2) around 1600 UT, the north magnetic pole leaned toward the dayside, whereas the south magnetic pole toward the nightside due to the offset between the magnetic and geographic poles, which makes the northern

auroral zonal extending further equatorward in the northern hemisphere than in the southern hemisphere along 70°W. Finally, in order to examine if dynamo fields are generated by the disturbed neutral winds during the storm, Figure 8c shows the difference plot of zonal ion drift due to the electric fields. Indeed, we find very little change in the zonal ion drift during the storm. The ineffectiveness for neutral winds to generate a disturbance dynamo field on the dayside during this particular storm could be explained by the relatively large *E*-region conductivities that effectively short out the F-region dynamo driven currents, a mechanism proposed by *Rishbeth* [1997].

4. Conclusion

The excellent observations by the Millstoen Hill and Arecibo radars during a geomagnetic storm have provided another opportunity to put the TIEGCM into the test. Although it was a moderate event with a minimum *Dst* value of ~70 nT and a maximum *AE* value of 2500 nT, the ionosphere yet exhibited some very unique characteristics, such as the peculiar UT-altitude profile of the *F*-region electron density that closely resembles the Greek letter Λ. Through the detailed data-model comparison, we have shown that the coupled AMIE-TIEGCM is able to reproduce many observed storm features of the ionospheric disturbances, including the Λ structure. The primary cause of this peculiar structure of the dayside positive storm phase is the storm-enhanced meridional neutral wind. The enhanced Joule heating in the high-latitude auroral zone produced a strongly equatorward/southward meridional wind surge that pushes plasma upward at mid latitudes. The subsequent northward wind associated with the rarefaction waves then pushed the ions downward, causing the peak height to drop. The neutral wind surges propagated in the form of gravity waves at a phase speed of ~700 m/s, consistent with the time delay observed between the two radars. The detailed component analysis of the simulation results reveals no significant dynamo electric fields produced by the wind surges in this case study. Our simulations also confirm that both composition changes and the

penetration magnetospheric electric fields play a very minor role in producing the observed positive storm phase.

It is worthy pointing out an earlier study by *Roble et al*. [1978] in which they showed that both Millstone Hill and Arecibo radars observed a strong positive storm phase with a very similar Λ structure in the electron density profile as in this case. Using a simplified 2-D ionospheric model, they concluded that the positive storm phase was produced by gravity waves generated by enhanced Joule and particular heating over the polar cap region. Our study presented here is fully consistent with their findings, and reiterates the importance of neutral wind effects on ionospheric disturbances.

Acknowledgments. We are grateful to many colleagues in providing the various satellite and ground based data which have used in AMIE for this study. The ACE data were obtained from the NASA CDAW website. The work at HAO was support in part by the NASA Sun-Earth Connection Guest Investigator program. Work at Haystack Observatory was supported under the NASA grant NAG5-13602. NCAR is sponsored by the NSF. Millstone Hill radar observations and analysis are supported by a NSF cooperative agreement with MIT. The Arecibo Observatory is operated by Cornell University with support from a cooperative agreement with the NSF. Others???

References

Blanc, M, and A. D. Richmond (1980), The ionospheric disturbance dynamo, *J. Geophys. Res., 8*5, 1669-1686.

Buonsanto, M. J. (1999), Ionospheric storms – A review, *Space Sceince Reviews, 88*, 563-601.

Burns, A. G., T. L. Killeen, G. R. Carignan, and R. G. Roble (1995), Large enhancements in the O/N2

ratio in the evening sector of the winter hemisphere during geomagnetic storms, *J. Geophys. Res., 100*, 14,661-14,671.

Chamberlin, P. C., T. N. Woods, and F. G. Eparvier, Flare Irradiance Spectral Model (FISM): Daily component algorithms and results, *Space Weather*, 5, S07005, doi:10.1029/2007SW000316, 2007.

Field, P. R., H. Rishbeth, R. J. Moffett, D. W. Idenden, T. J. Fuller-Rowell, G. H. Millward, and A. D. Aylward (1998), Modeling composition changes in F-layer storm, *J. Atmos. Solar-Terr. Phys., 60*, 523-543.

Goncharenko, L. P., J. C. Foster, A. J. Coster, C. Huang, N. Aponte, and L. J. Paxston (207), Observations of a positive storm phase on September 10, 2005, *J. Atmos. Solar-Terr. Phys. 69*, 1253-1272.

Hagan, M. E., and J. M. Forbes (2002), Migrating and nonmigrating diurnal tides in the middle and upper atmosphere excited by tropospheric latent heat release, J. *Geophys. Res., 107*(D24) 4754, doi:10.1029/2001JD001236.

Huang, C.-S., J. C. Foster, and M. C. Kelley (2005a), Long-duration penetration of the interplentary electric field to the low-latitude ionosphere during the main phase of magnetic storms, *J. Geophys. Res., 110*, A11309, doi:10.1029/2005JA011202.

Huang, C.-S., J. C. Foster, L. P.Goncharenko, P. J. Erickson, and W. Rideout (2005b), A strong positive phase of ionospheric storms observed by the Millstone Hill incoherent scatter radar and global GPS network, *J. Geophys. Res., 110*, A06303, doi:10.1029/2004JA010865.

Lu, G., et al. (1996), High-latitude ionospheric electrodynamics as determined by the assimilative mapping of ionospheric electrodynamics procedure for the conjunctive SUNDIAL/ATLAS 1/GEM period of March 28-29, 1992, *J. Geophys. Res., 101*, 26,697-26,718.

Mannucci, A. J., B. T. Tsurutani, B. A. Iijima, A. Komjathy, A. Saito, W. D. Gonzales, F. L.Guarnieri, J. U. Kozyra, and R. Skoug (2005), Dayside global ionospheric response to the major interplanetary events of October 29-30, 2003 “Holloween Storms”, *Geophys. Res. Lett., 32*, L12S02, doi:10.1029/2004GL021467.

Maruyama, N., A. D. Richmond, T. J. Fulle-Rowell, M. V. Codrescu, S. Sazykin, F. R. Toffoletto, R. W. Spiro, G. H. Millward (2005), Interaction between direct penetration and disturbance dynamo electric fields in the storm-time equatorial ionosphere, *Geophys. Res. Let*t., 32, L17105, doi:10.1029/2005GL023763.

Prolss, G. W. (1993), On explainating the local time variation of ionospheric storm effects, *Ann. Geophys.* 1-9.

Prolss, G. W. (1995), Ionospheric F-region storms, in handbook of Atmospheric Electrodynamics,

edited by H. Valland, CRC Press, Boca Roton, FL.

Richmond, A. D., and Y. Kamide (1988), Mapping of ionospheric electrodynamic features of the high-latitude ionosphere from localized observations, *J. Geophys. Res., 93*, 5741-5759.

Richmond, A. D.,E. C. Ridley, and R. G. Roble (1992), A thermosphere/ionosphere general circulation model with coupled electrodynamics, *Geophys. Res. Lett., 19*, 601-604.

Rishbeth, H. (1997), The ionospheric E-layer and F-layer dynamo – a tutorial review, J. *Atmos. Solar-Terr. Phys., 99*, 1873-1880.

Rishbeth, H. (1989), F-region stormsand thermospheric circulation, in *Electromagneitic Coupling in the Polar Clefts and Caps*, edited by P. E. Sandholt and A. Egeland, 393-406, Kluwer Acad., Norwell, MA.

Roble, R. G., A. D. Richmond, W. L. Oliver, and R. M. Harper (1978), Ionospheric effects of the gravity wave launched by the September 18, 1974, suddden commencement, *J. Geophys. Res*., 83, 999-1009.

Schunk, R. W., and A. F. Nagy (2000), Ionospheres – Physics, Plasma Physics, and Chemistry, Cambridge Univefsity Press.

Tsurutani, B., et al. (2004), Global dayside ionospheric uplift and enhancement associated with interplanetary electric fields, *J. Geophys. Res., 109*, A08302, doi:10.1029/2003JA010342.

Figure Captions

Fgiure 1. Distributions of (a) the IMF B_z component, (b) solar wind dynamic pressure, (c) the *Dst* index, (d) the *AE* index, (e) the cross-polar-cap electric potential drop in the northern (solid line) and southern (dashed line) hemisphere, and (f) the hemispheric integrated Joule heating over the northern hemisphere (solid line) and southern (dashed line) and the northern hemispheric integrated auroral power (dotted line). The vertical dashed line marks the onset of geomagnetic storm at about 1600 UT on 10 September.

Figure 2. UT-altitude profiles of measured electron density (top row), simulated electron density (2nd row), measured eletron temperature (3rd row), simulated electron temperature (4th row), measured vertical ion drift (5th row), simulated vertical ion drift (bottom row) for the quiet day on 8 September (left column) and for storm day on 10 Spetember (right column), over Millstone Hill. The vertical dashed line denotes the onset of upward lift of electron density peak height.

Figure 3. Similar to Figure 2, but over Arecibo.

Figure 4. Comparison of GPS TEC measurements and the simulated TEC distributions.

Figure 5. Comparison of GUVI and TIEGCM percent difference O/N2 ratio.

Figure 6. Percent difference plots of electron density (top row) and O/N_2 (bottom row). The left column is for Millstone Hill, and the right column for Arecibo.

Figure 7. Simulated UT-altitude profiles of meridional wind (top row), vertical ion drift due to neutral wind (2^{nd} row), and vertical ion drift due to electric field (bottom row). The vertical dashed lines mark the onset of the uplift of electron density at Millstone Hill (left column) and Arecibo (right column).

Figure 8. Simulated difference plots of (a) meridional wind, (b) vertical ion drift compoment due to neutral wind, (c) zonal ion drift due to electric field.

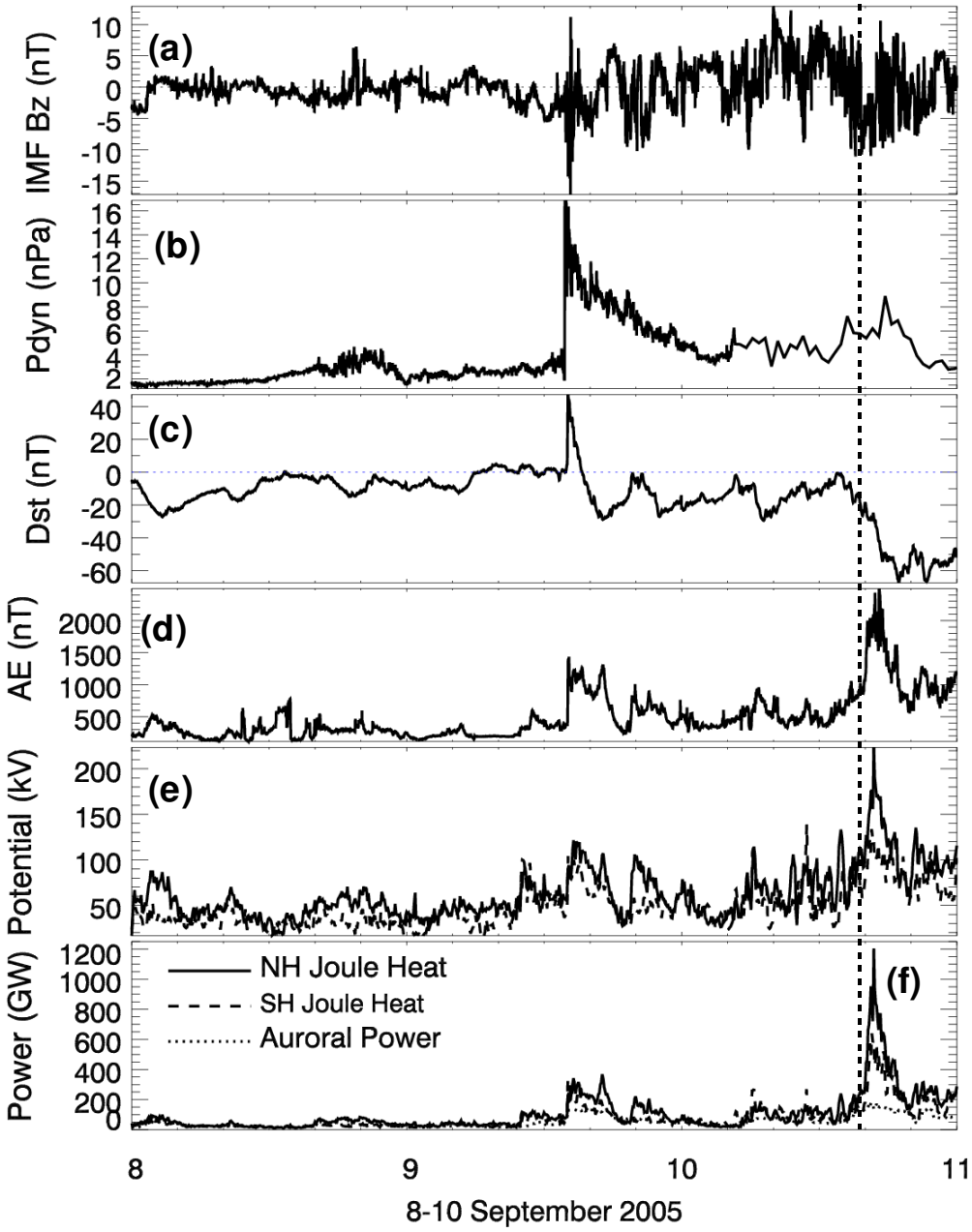
(a)
IMF Bz (nT)
10
5
0
-5
-10
-15
(b)
Pdyn (nPa)
16
14
12
10
8
6
4
2
(c)
Dst (nT)
40
20
0
-20
-40
-60
(d)
AE (nT)
2000
1500
1000
500
(e)
Potential (kV)
200
150
100
50
(f)
Power (GW)
1200
1000
800
600
400
200
0
NH Joule Heat
SH Joule Heat
Auroral Power
8
9
10
11
8-10 September 2005

Fgiure 1

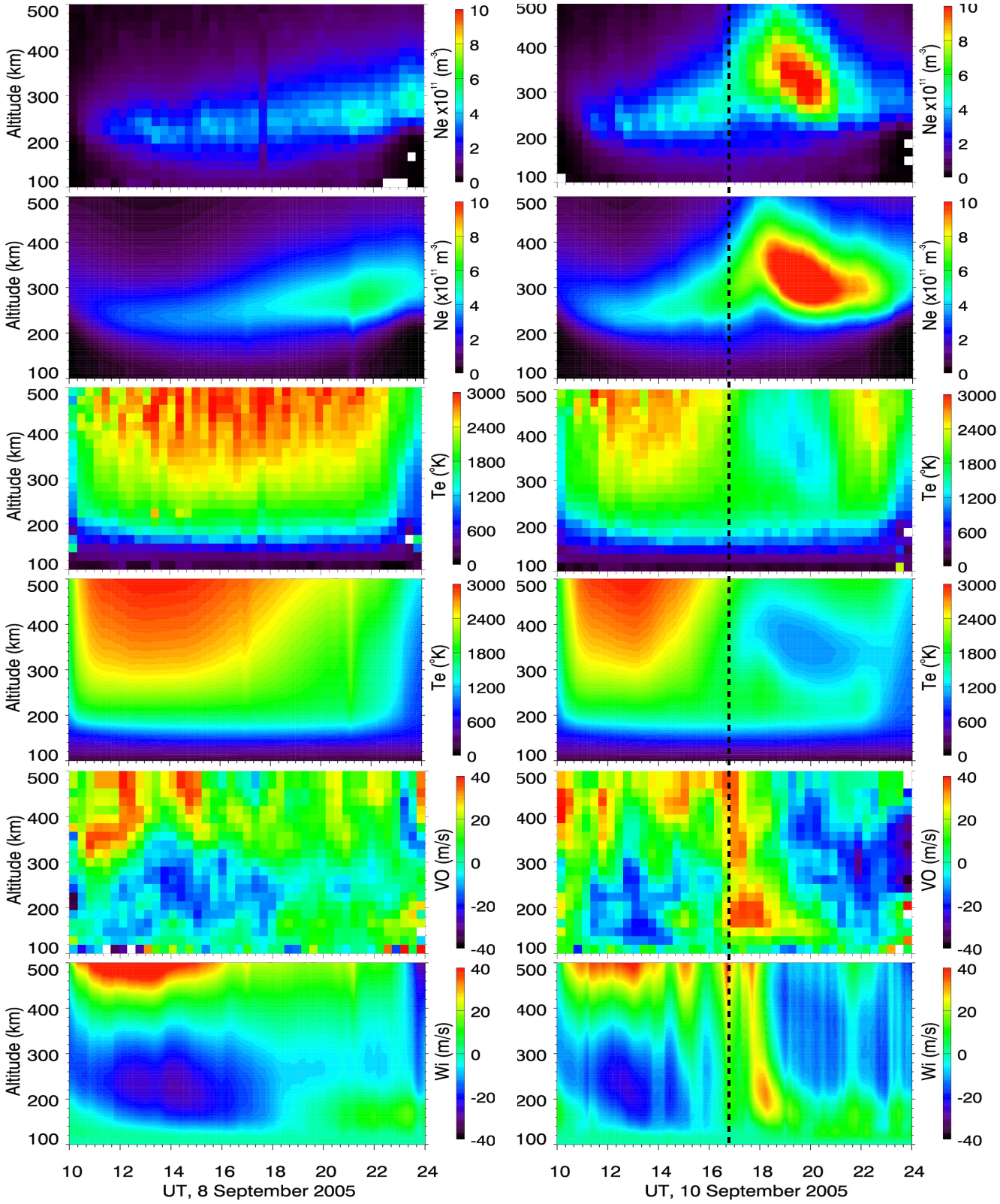
Altitude (km)
Ne x10^11 (m^-3)
Ne (x10^11 m^-3)
Te (°K)
VO (m/s)
Wi (m/s)
UT, 8 September 2005
UT, 10 September 2005

Fgiure 2

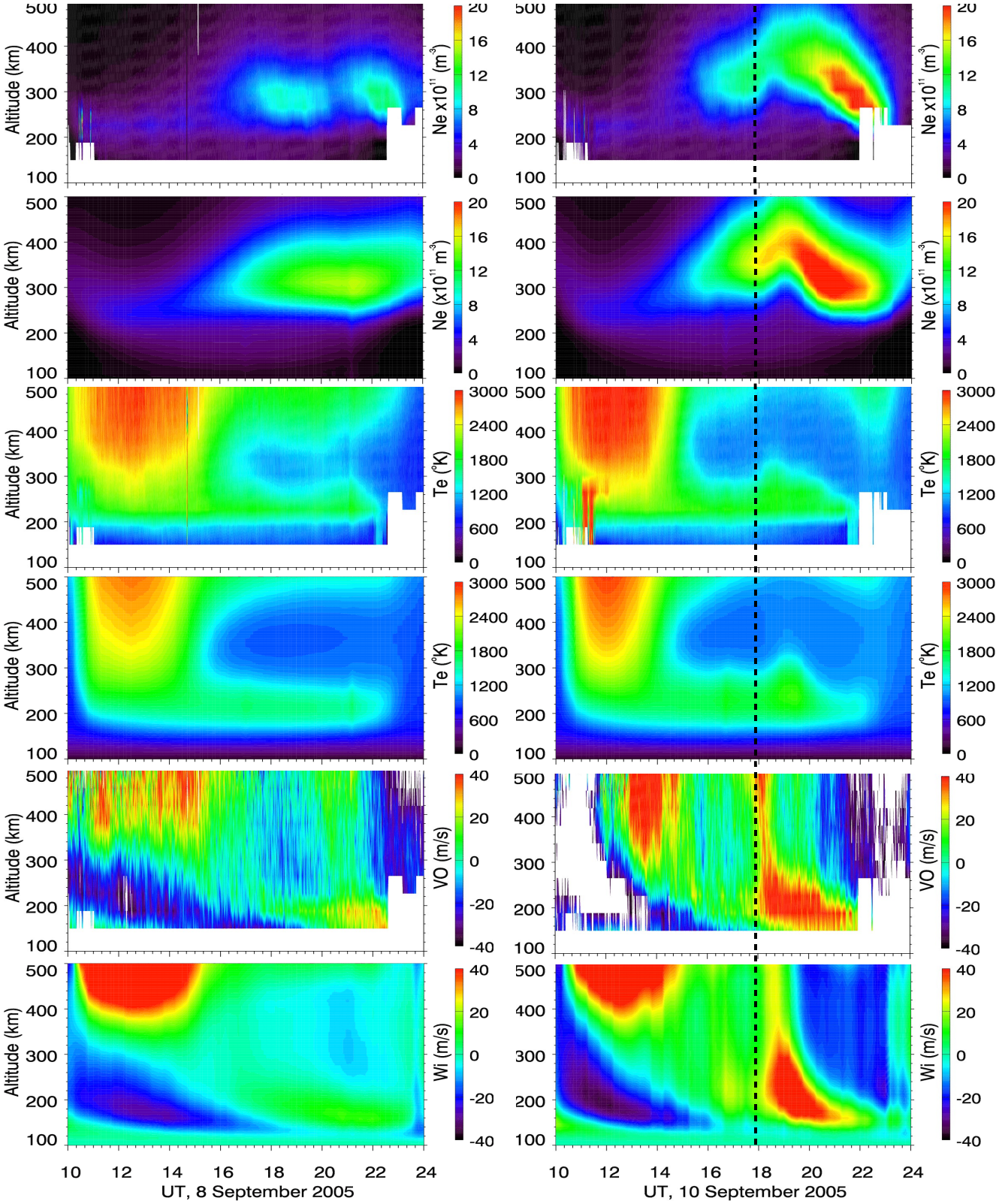
Altitude (km)
Ne x10^11 (m^-3)
Ne (x10^11 m^-3)
Te (°K)
VO (m/s)
Wi (m/s)
UT, 8 September 2005
UT, 10 September 2005

Figure 3

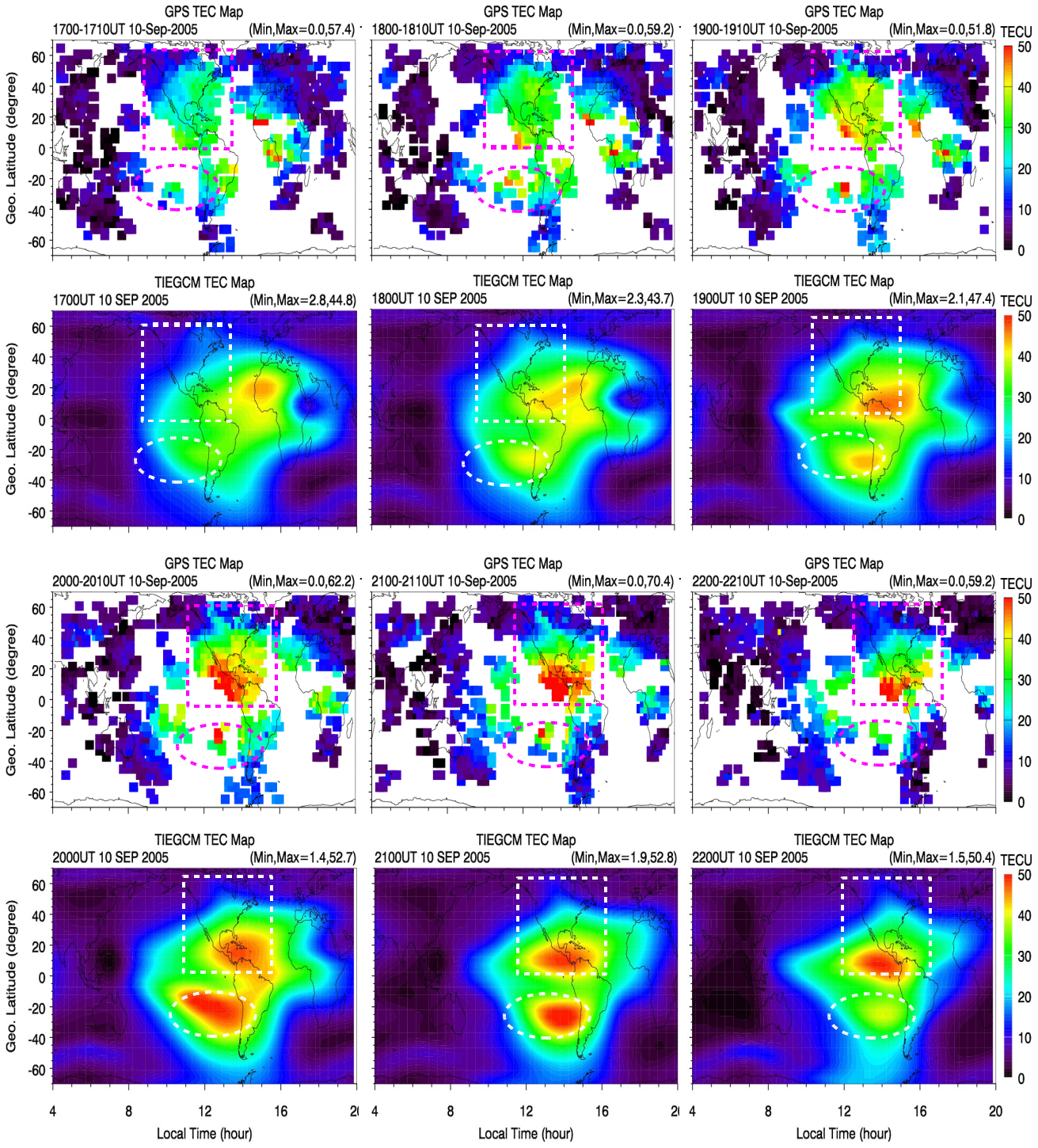
GPS TEC Map
1700-1710UT 10-Sep-2005 (Min,Max=0.0,57.4)
GPS TEC Map
1800-1810UT 10-Sep-2005 (Min,Max=0.0,59.2)
GPS TEC Map
1900-1910UT 10-Sep-2005 (Min,Max=0.0,51.8)
TECU
TIEGCM TEC Map
1700UT 10 SEP 2005 (Min,Max=2.8,44.8)
TIEGCM TEC Map
1800UT 10 SEP 2005 (Min,Max=2.3,43.7)
TIEGCM TEC Map
1900UT 10 SEP 2005 (Min,Max=2.1,47.4)
GPS TEC Map
2000-2010UT 10-Sep-2005 (Min,Max=0.0,62.2)
GPS TEC Map
2100-2110UT 10-Sep-2005 (Min,Max=0.0,70.4)
GPS TEC Map
2200-2210UT 10-Sep-2005 (Min,Max=0.0,59.2)
TIEGCM TEC Map
2000UT 10 SEP 2005 (Min,Max=1.4,52.7)
TIEGCM TEC Map
2100UT 10 SEP 2005 (Min,Max=1.9,52.8)
TIEGCM TEC Map
2200UT 10 SEP 2005 (Min,Max=1.5,50.4)
Geo. Latitude (degree)
Local Time (hour)

Figure 4

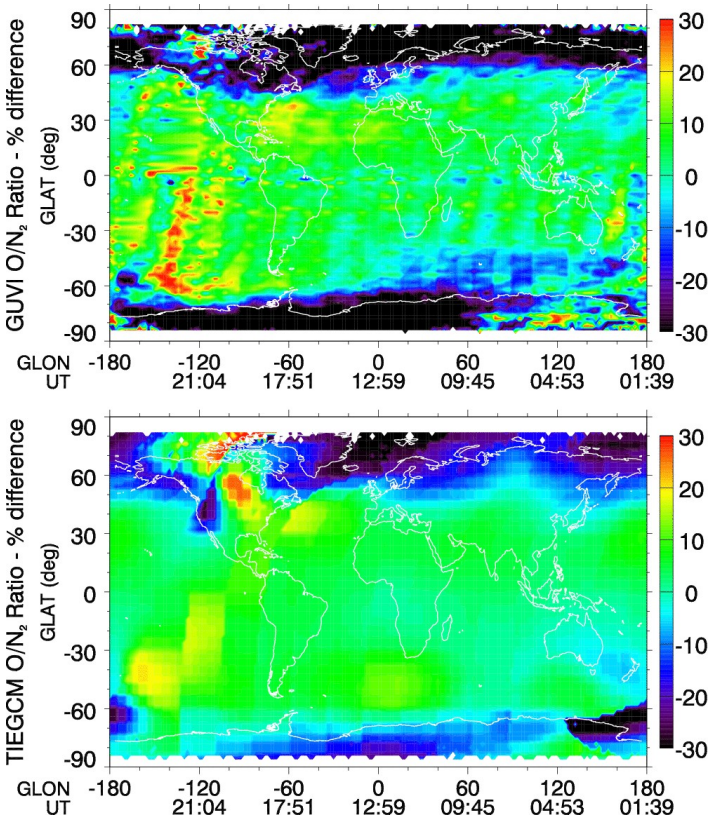
GUVI O/N2 Ratio - % difference
TIEGCM O/N2 Ratio - % difference
GLAT (deg)
90
60
30
0
-30
-60
-90
30
20
10
0
-10
-20
-30
GLON
UT
-180
-120
21:04
-60
17:51
0
12:59
60
09:45
120
04:53
180
01:39

Figure 5

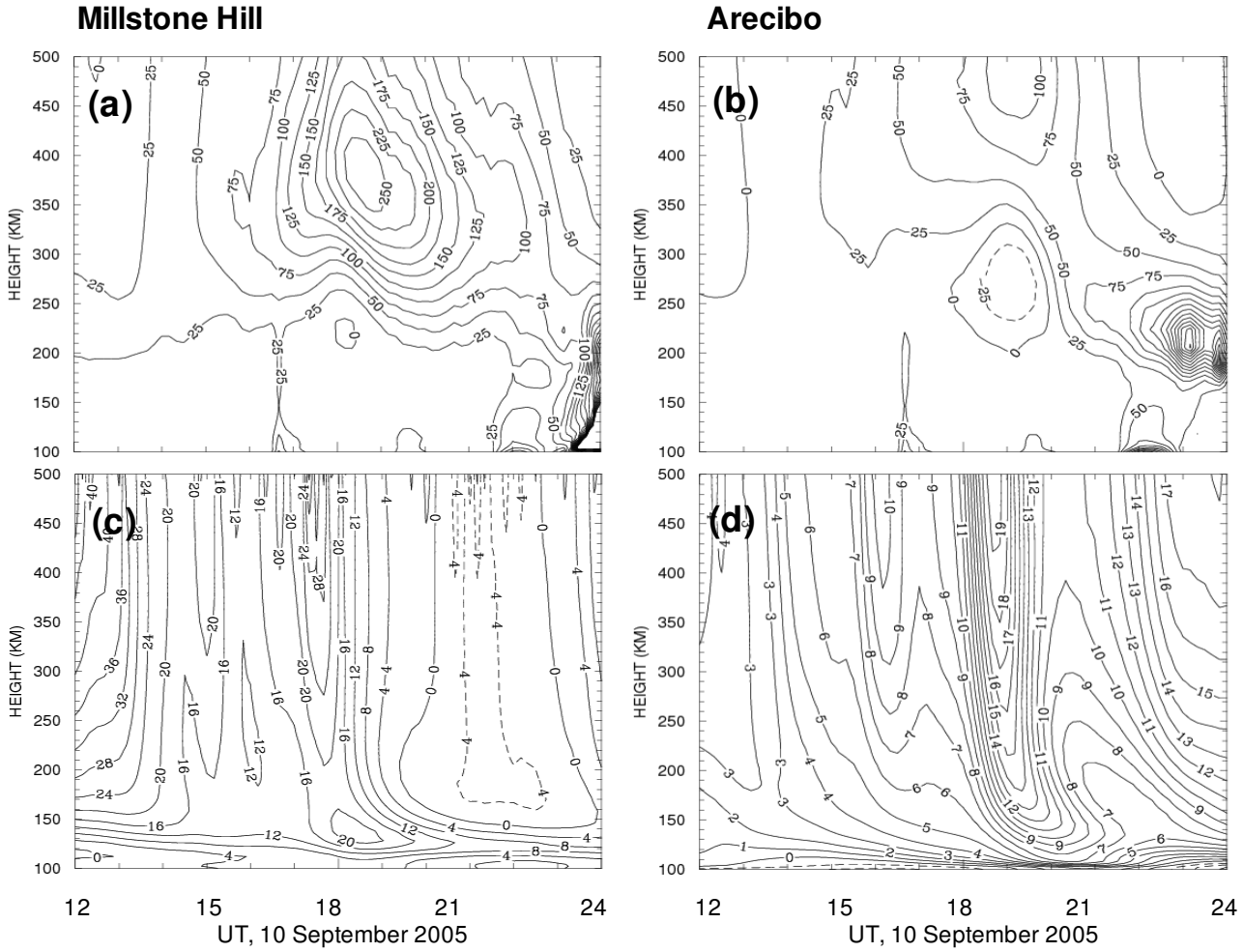

Figure 6

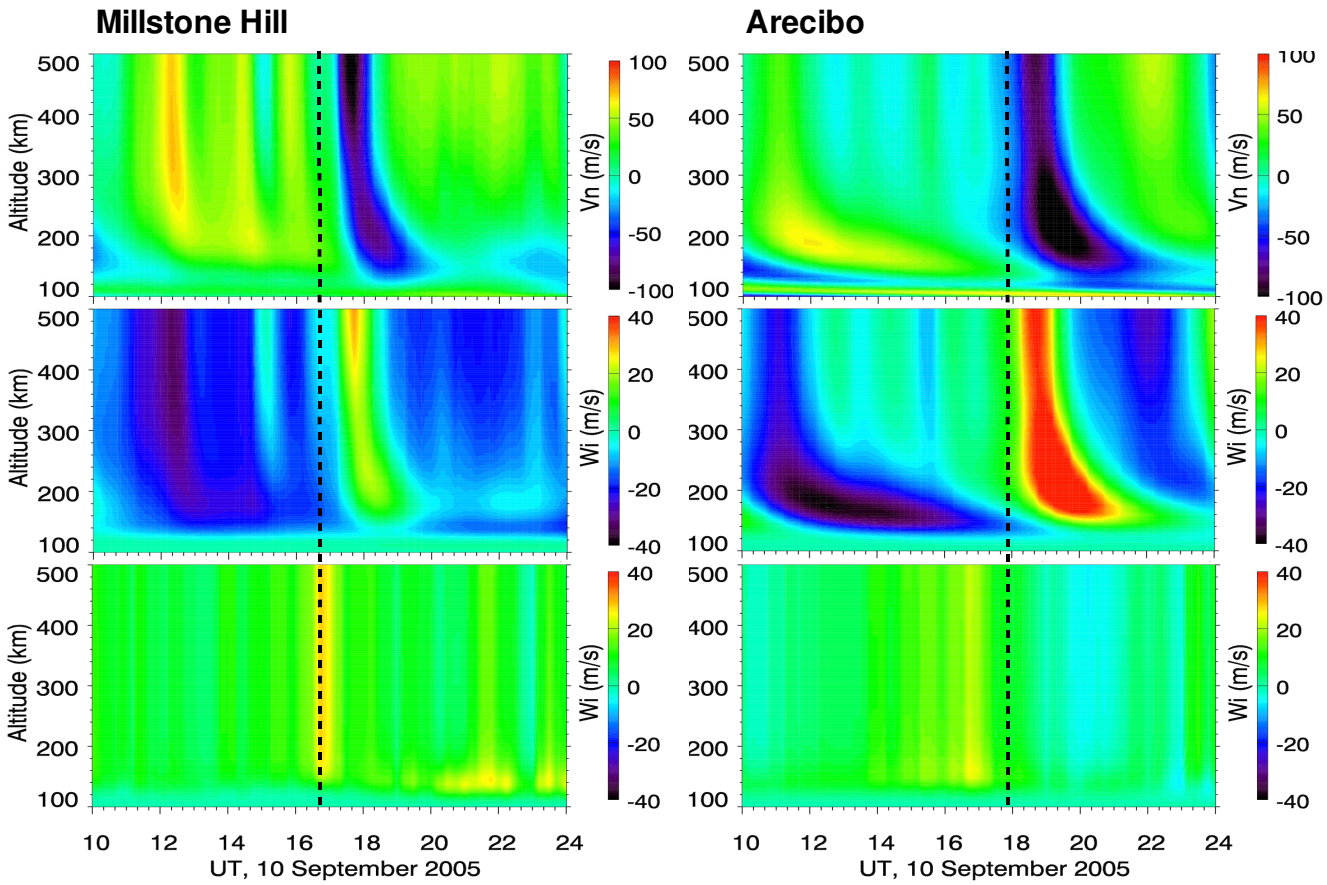
Millstone Hill
Arecibo
Altitude (km)
Vn (m/s)
Wi (m/s)
UT, 10 September 2005

Figure 7

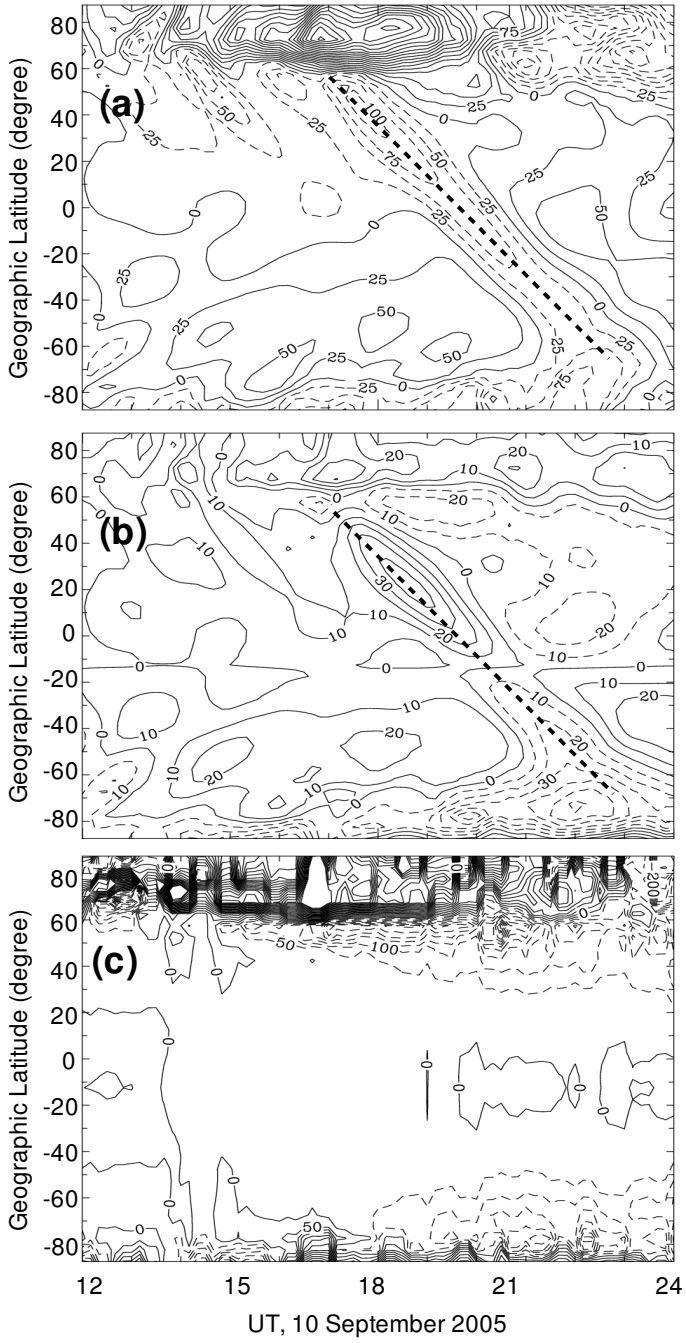
(a)
(b)
(c)
Geographic Latitude (degree)
UT, 10 September 2005
12
15
18
21
24

Figure 8